

Chapter 2

High Temperature Cuprate Superconductors

Abstract When Bednorz and Müller discovered the superconductivity in a compound La-Ba-Cu-O in 1986, it was considered as a breakthrough in the research of the superconductivity. This leads to the discovery of the other cuprate superconductors, and immediately the transition temperature of the synthesized materials reached to the liquid nitrogen temperature. Today the maximum transition temperature of the cuprate superconductors changes from 35 K for $\text{La}_{2-x}\text{Sr}_x\text{CuO}_4$ to 138 K for $\text{Hg}_{1-x}\text{Tl}_x\text{Ba}_2\text{Ca}_2\text{Cu}_3\text{O}_y$ (the highest record under normal pressure, which extends to ~ 160 K at high pressure) [1].

2.1 General Properties of Cuprates

2.1.1 Crystal Structure

As a common property, all cuprate superconductors have a layered perovskite structure that consists of alternating conducting CuO_2 layers and insulating blocking layers that provide charge carriers to the CuO_2 layers. Even though this is the general scheme, the numbers of the CuO_2 layers are different in different cuprate families. In Fig. 2.1, as an example to 1-, 2-, and 3- layer cuprate families had been shown.

In this thesis, we worked with double layer $\text{YBa}_2\text{Cu}_3\text{O}_y$ system, because the additional structures, namely the CuO-chains in this system give some advantage in our measurements by increasing the conductivity along the c -axis.

$\text{YBa}_2\text{Cu}_3\text{O}_y$ is a system, where the charge doping can be adjusted with oxygen annealing. And this material belongs to the hole doped case, where we will show the electronic phase diagram in the next section. In cuprates, it is also possible to create hole doping in the system with substituting positive ions by ions of smaller valence, such as Sr^{2+} to La^{3+} sites in $\text{La}_{2-x}\text{Sr}_x\text{CuO}_4$. Zn-substitution that been used in this study, on the other hand does not alter the doping level.

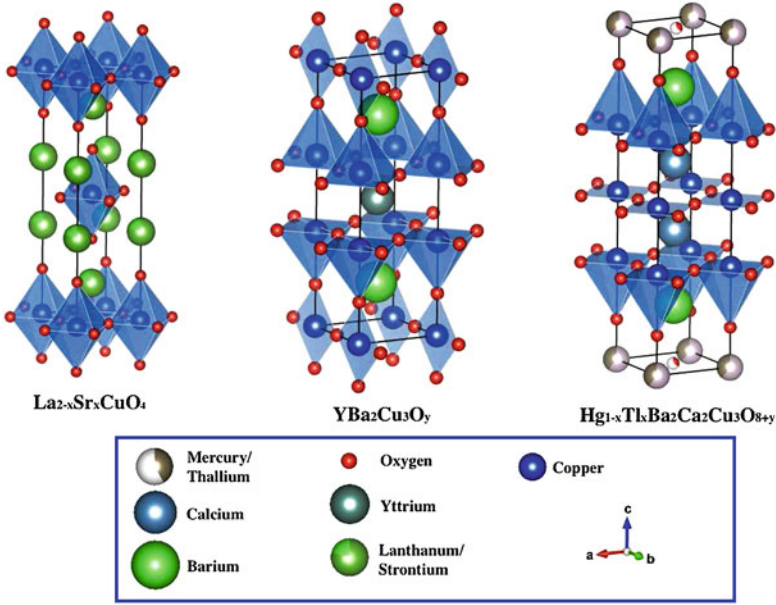


Fig. 2.1 Crystal structure of 1 ($\text{La}_{2-x}\text{Sr}_x\text{CuO}_4$ [2]), 2 ($\text{YBa}_2\text{Cu}_3\text{O}_y$ [3]), and 3 ($\text{Hg}_{1-x}\text{Tl}_x\text{Ba}_2\text{Ca}_2\text{Cu}_3\text{O}_{8+y}$ [1]) layer cuprates

2.1.2 Phase Diagram

Phase diagram of the cuprate superconductors can be divided into two as the electron doped and the hole doped side. In Fig. 2.2, phase diagram of the hole doped and electron doped cuprate superconductors had been shown. The electron doped case is not the topic of this thesis; therefore, the hole doped side of the phase diagram will be explained in more detail.

The so-called parent compound in cuprates (for instance non-doped $\text{YBa}_2\text{Cu}_3\text{O}_6$ for $\text{YBa}_2\text{Cu}_3\text{O}_y$, hole concentration is zero) is an antiferromagnetic Mott insulator. The Néel temperature is around 350 K. With hole doping to the system, the antiferromagnetic insulator state is rapidly suppressed and around 5 % doping superconductivity starts to be observed.

The superconducting dome is another common behavior among the cuprate families, even though the transition temperature differs greatly from around 35–138 K. The maximum T_c will be observed around 16 % doping level that is referred as the optimally doped region.

The doping region between 5 and 16 % is called the underdoped region. The normal state of this region is the strange metal region, which is characterized by the pseudogap. Although this region is metallic in the normal state, it cannot be defined as the conventional Fermi liquid region, hence it is referred as the strange metal region.

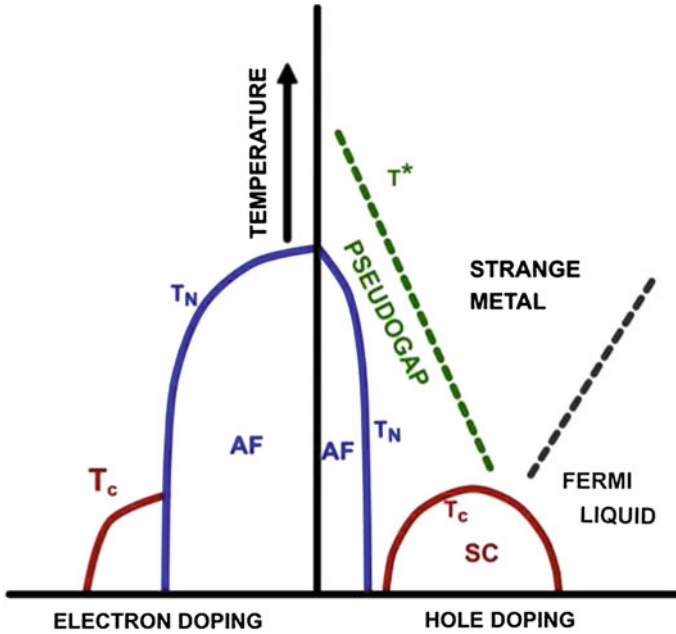


Fig. 2.2 Phase diagram of the cuprate superconductors

Pseudogap region, where a partial gap in the density of states at the Fermi surface had been observed by several experimental probes, is one of the issues in the phase diagram. The pseudogap state strongly dominates the underdoped region with a behavior that is mostly agreed among different probes. On the other hand, some debates still continue about the behavior in the overdoped region. Pseudogap state is one of the main topics of this thesis in Chap. 4.

Beyond the optimum hole doping region, system is referred as overdoped. In the overdoped region system is getting closer to the Fermi-liquid state. In the heavily overdoped regime, it can be defined with the conventional Fermi-liquid theory.

2.1.3 Electronic Structure of Cuprates

It is well known that the superconductivity arises in the CuO_2 planes in the cuprate superconductors. Cu atoms are surrounded by six oxygen atoms creating an octahedral form (Fig. 2.3a, here the apical oxygens has not been shown). In this case the Cu band is half filled with a single hole that has spin 1/2. The Jahn-Teller distortion of this octahedral form (due to the apical oxygens) leads a splitting in the Cu energy states to e_g ($d_{x^2-y^2}$ and $d_{3z^2-r^2}$) (Fig. 2.3b), where the highest partially occupied d states is the $d_{x^2-y^2}$. Oxygen p states also split and a hybridization of these states

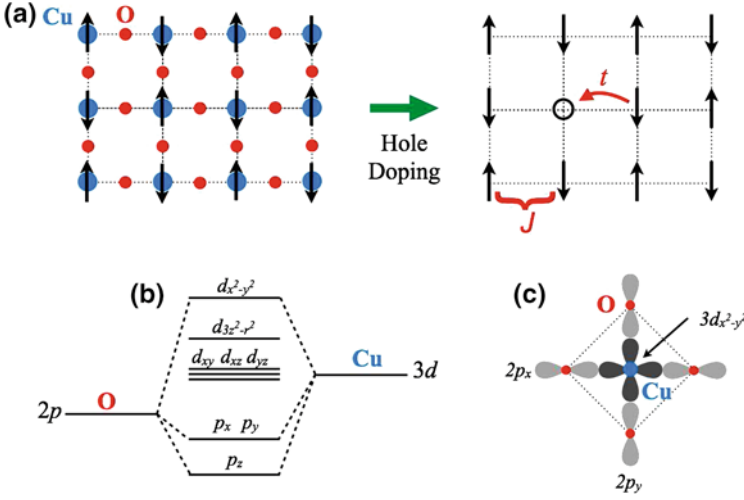


Fig. 2.3 **a** Schematic picture of the CuO_2 plane in the parent compound and in the case of hole doping. **b** Schematic diagram for the energies of Cu $3d$ and O $2p$ orbitals. **c** Hybridization of Cu $3d$ and O $2p$ orbitals

will be observed (Fig. 2.3c). Thus the electronic state of the cuprates can be described by the three-band model including the Cu $d_{x^2-y^2}$ and O p_x and p_y [4, 5].

Due to the partially gapped d -band, band structure calculations predict that the system is a metal, however, the parent compound of the cuprates shows insulating behavior (Mott insulator). It is insulating because the Coulomb repulsion U (a few eV between upper and the lower Hubbard band) on the Cu-sites are larger than the bandwidth. More precisely these compounds can be classified as the charge transfer insulators, because the lowest energy excitations, charge transfer excitations, are smaller than the on-site Coulomb repulsion, U .

It is believed that many aspects of the physics of the cuprates can be explained with a single band Hubbard model [6], which contains a kinetic energy term, t , and a Hubbard term, U . Here t is proportional to the nearest neighbor hopping amplitude and U defines the electron correlations. In the strong coupling limit at half filling (parent compound), where $U \gg t$, electrons tend to localize, hence we observe the insulating behavior. Since we have a localized system, as one unpaired electron on each unit cell with the spin $+1/2$ or $-1/2$, the configurations of the neighboring electrons determine the stability of the system. The antiparallel order of the spins is the chosen state, since this state allows the electrons to penetrate other sites with exchange process. In the parallel ordering, the exchange mechanism is prohibited due to the Pauli exclusion principle and there is no gained energy (J). Under this circumstances the hamiltonian of the system can be defined with the t - J model and given as:

$$\mathcal{H}_{\text{Hubbard}} = -t \sum_{i,j,\sigma} c_{i\sigma}^\dagger c_{j\sigma} + J \sum_{i,j} (\mathbf{S}_i \cdot \mathbf{S}_j - \frac{n_i n_j}{4}) \quad (2.1)$$

Here, J is the exchange energy, which also includes the Coulomb term. \mathbf{S}_i and \mathbf{S}_j are the spins in the site i and site j . When we start to dope holes to the Mott insulator, the situation becomes rather complicated. In the low doping level (non-superconducting state), when the kinetic term becomes dominant in one site, the electrons become itinerant. However, if the electron transferred to a vacant site has the spin with the same order with the neighboring site, the exchange energy will be destabilized, while the electronic energy will be stabilized. The condition between J and t will determine the result.

With further hole doping (the region that we start to see the superconductivity) the antiferromagnetic order loses its stability and system starts to become metallic and superconductive. The Hubbard gap starts to close and with further doping it closes completely and a well-defined Fermi surface will be formed. In this case, the system shows Fermi-liquid behavior. However, there is no consensus about the electronic structure in the intermediate region, between the two extreme points. There are some theories, which try to explain this intermediate region with doped Mott insulator scenario, while others suggest that the difficulties seen in this region can be solved with modifications on Fermi-liquid theory (modified Fermi-liquid approach).

Although the BCS theory successfully explains the microscopic features for the conventional superconductors, it is quite insufficient to explain those of the high-temperature superconductors. Nevertheless, there is not a generally established theory for these materials. It seems that not only the superconducting state but also other regions of the phase diagram show interesting and unusual features. Therefore, the microscopic theories proposed for HTSCs are expected to explain these regions, too. There have been many theories proposed over the years. Some of these theories can be given as: Resonating Valance Bond (RVB) theory [7, 8], Spin fluctuations [9, 10] and Inhomogeneity induced pairing [11]. However, none of these theories can explain the phase diagram of the cuprate high temperature superconductors.

2.2 Pseudogap and Precursor Superconducting State

2.2.1 Pseudogap State

Pseudogap state has been observed by many experimental probes as the partial gap in the Fermi surface. In this section, a summary will be given on the techniques that presented the pseudogap behavior in the high temperature cuprate superconductors. Despite the variety of the probes and experiments, the origin of the pseudogap and its relation with the superconducting region is still controversial. Although there are a variety of theories, it seems they can be summarized in two main ideas: The one that explains the pseudogap as a precursor of superconductivity, and the other that presents this state as the competing order to the superconductivity.

The first technique that observed the existence of the pseudogap was the nuclear magnetic resonance (NMR) probe. The spin channel can be observed with this probe.

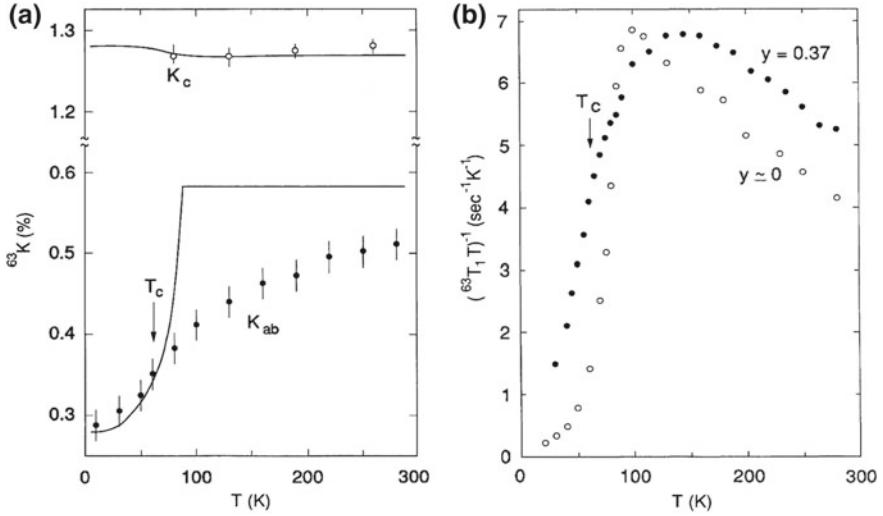


Fig. 2.4 **a** Cu Knight shift and **b** Cu relaxation rate for YBa₂Cu₃O_{7-y} with $y = 0$ (optimally doped) and $y = 0.37$ (underdoped). Reprinted with permission from Ref. [12]. Copyright (1991) by the American Physical Society

Therefore, this had been used as the evidence that the pseudogap is a spin density wave. On the other hand, the pseudogap had been observed in a charge channel, as well. The optical conductivity, which is the topic of this thesis, is one of these probes.

Pseudogap had been observed in Knight shift, K_s and spin-lattice relaxation rate, $1/T_1$. Both the Knight shift and the relaxation rate show a decrease below T_c indicating the superconducting transition. Some examples are shown in Fig. 2.4 for two different doping levels, namely for the optimally doped and for the underdoped region. For the optimally doped sample the decrease of the Knight shift and relaxation rate below T_c is observed. For the underdoped sample, on the other hand, the behavior is dramatically different. The decrease of K_s and $1/T_1$ start well above T_c , that is even decrease to its 20 % above T_c . This had been attributed to the pseudogap behavior. The data in Fig. 2.4 belongs to the Cu ion. However, it has been shown that a similar behavior was also observed for other ion sites such as ^{89}Y , as well [13].

The ARPES measurements pointed out that the pseudogap dominates the antinodal region of the Fermi surface. Therefore, to use a momentum dependent technique is an advantage. The pseudogap had been observed for many cuprate families with ARPES. Bi-systems among them are the ones that were extensively studied. Due to the surface conditions these systems are the most suitable ones. In Fig. 2.5, the temperature dependent ARPES spectra are shown for the Bi₂Sr₂Ca₂Cu₃O_{10+ δ} sample in the antinodal region. As can be seen more easily from the symmetrized spectra (Fig. 2.5b), the gap closes at temperatures above T_c .

Some other ARPES results were also discussed in terms of the pseudogap behavior below the superconducting transition temperature. The sharp peak in the spectra had

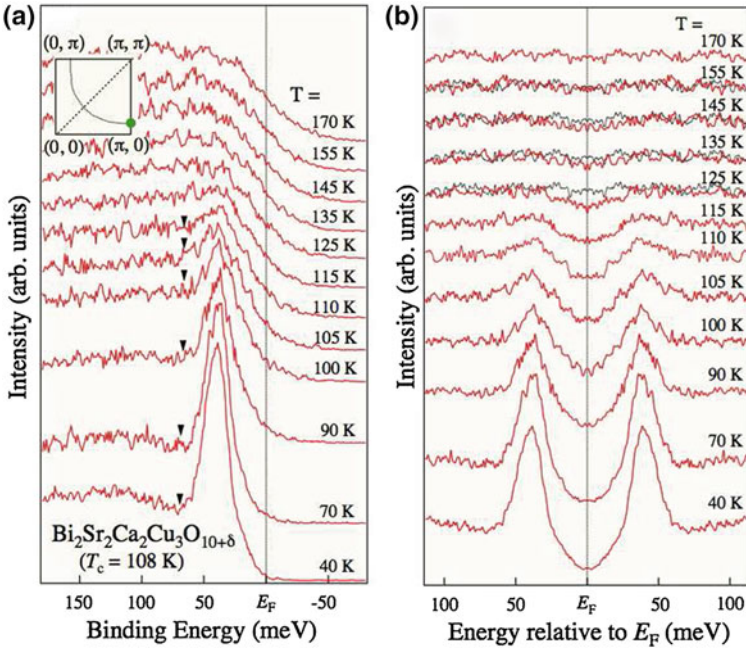
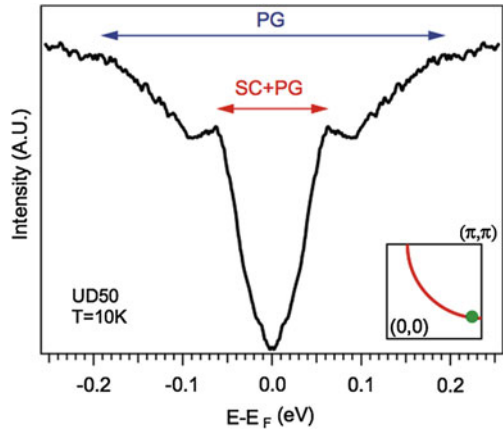


Fig. 2.5 **a** Temperature dependence of ARPES spectra. **b** Symmetrized ARPES spectra. Reprinted with permission from Ref. [14]. Copyright (2002) by the American Physical Society

Fig. 2.6 A low-energy peak associated with superconductivity (SC) and a broader feature at higher energy associated with the pseudogap (PG). This data belongs to underdoped sample. Reprinted with permission from Ref. [15]. Copyright (2010) by the Institute of Physics Publishing and Deutsche Physikalische Gesellschaft



been associated with the superconducting gap. Moreover, the broad feature at the higher energies was attributed to the pseudogap. Two different energy scales support the scenario of two different gaps. Features of the superconducting gap and the pseudogap have been given in Fig. 2.6.

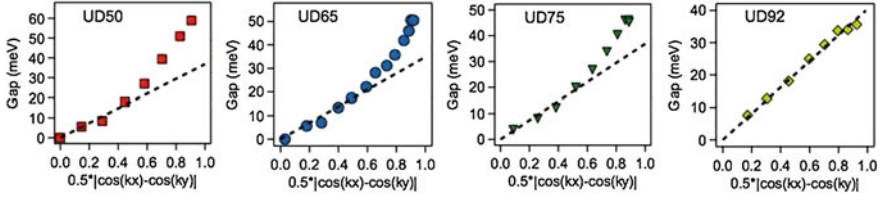


Fig. 2.7 Doping dependence of the momentum dependent SC gap function of $\text{Bi}_2\text{Sr}_2\text{CaCu}_2\text{O}_8$. Dashed lines are the simple d -wave function. Reprinted with permission from Ref. [15]. Copyright (2010) by the Institute of Physics Publishing and Deutsche Physikalische Gesellschaft

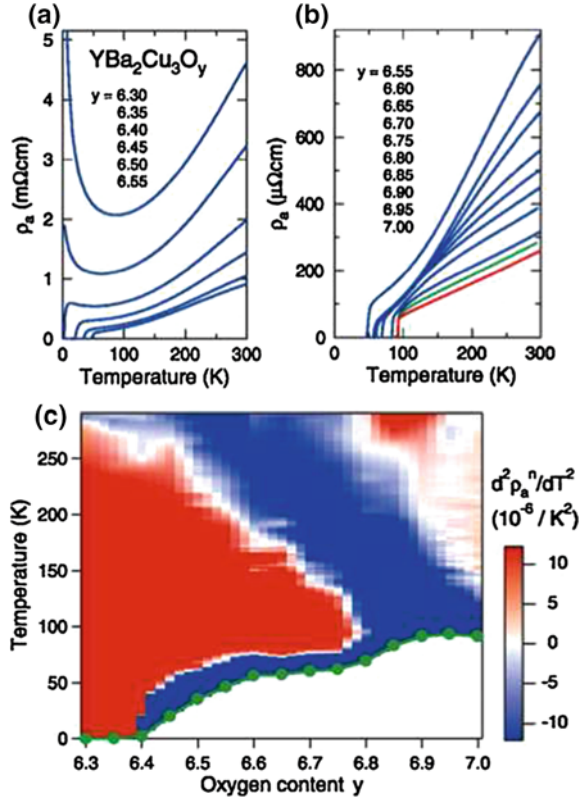
Moreover, some recent experiments showed that the gap function of the underdoped samples deviates from the d -wave form near the antinodal region, as is shown in Fig. 2.7. This can be explained if we assume that the pseudogap effect on the superconducting gap is getting stronger with underdoping (where the pseudogap is stronger). Therefore, the observed gap function in the antinodal region is not only the superconducting gap, but also the effects of the pseudogap. This explanation is based on the two gap scenario.

Pseudogap behavior was also observed in the transport measurements. One of the most extensive studies on the pseudogap behavior in the in-plane resistivity had been performed by Ando et al. [16]. They measured the in-plane resistivity of series of cuprate families over the very wide doping range of the phase diagram. In Fig. 2.8 the data of $\text{YBa}_2\text{Cu}_3\text{O}_y$ are presented. By using these resistivity data, Ando et al. map the in-plane resistivity curve. Furthermore, they define the pseudogap behavior as the inflection point of the resistivity curve (where the second derivative of T is zero). As a result, the pseudogap temperature derived with this method becomes the diagonal white line on the phase diagram (Fig. 2.8c).

Another way to define the pseudogap behavior has been recently proposed by Naqib et al. [17] on out-of-plane resistivity. In Fig. 2.9, the out-of-plane resistivity data for $\text{YBa}_2\text{Cu}_3\text{O}_y$ are shown. Black curves are the proposed theory based on the $t-J$ model calculations with some modifications. The fitting function is also on this figure. Here the first term defines the linear temperature-dependence, whereas, in the second term, β is a variable that depends on the c -axis tunneling matrix element and electronic density of states at high energies outside the pseudogap region. ε_g defines the pseudogap energy.

If we know the pseudogap energy, then we can convert it to temperature as $T = \varepsilon_g/k_B$. This conversion has been done for both $\text{YBa}_2\text{Cu}_3\text{O}_y$ and Ca-substituted $\text{YBa}_2\text{Cu}_3\text{O}_y$ (with Ca-doping we can achieve more overdoped region than the case of Ca-free samples). Results are given as a phase diagram in Fig. 2.10. As can be seen from this figure, for the most overdoped sample (nearly 19%), the pseudogap line crosses the T_c dome and goes to the quantum critical point. This will indicate that the pseudogap is not a precursor of superconductivity, but an independent order. On the other hand, despite the improved explanations, in-plane and out-of-plane resistivity curves give significantly different temperature scales for T^* (in-plane case

Fig. 2.8 Doping dependent in-plane resistivity curves for $\text{YBa}_2\text{Cu}_3\text{O}_y$ (a, b) and the resistivity curve mapping (c). Reprinted with permission from Ref. [16]. Copyright (2004) by the American Physical Society



30–40 % lower than out-of-plane). This can be explained with the explanation that the in-plane resistivity is sensitive to the nodal region of the Fermi surface, while the out-of-plane resistivity is sensitive to the antinodal region. In this case, it assumes that the pseudogap gradually opens from the antinodal region towards the nodal region with lowering temperature. Our optical data are mostly consistent with out-of-plane resistivity data.

The pseudogap behavior in the infrared spectra will be given in the next chapter in detail.

2.2.2 Precursor Superconducting State

Precursor superconductivity has been discussed by many experimental groups. Even though previously the pseudogap state was considered as a precursor of superconductivity, recent experimental results were of a favor of different order scenario. On the other hand, different experimental probes reported the existence of the

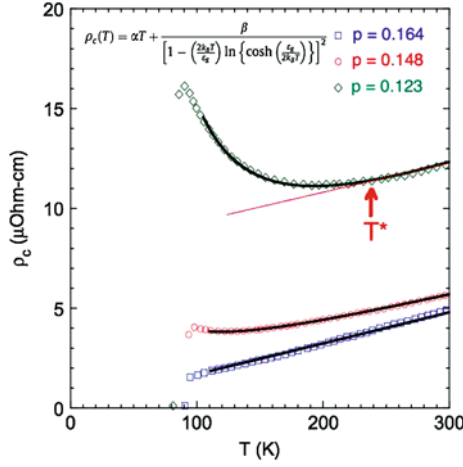
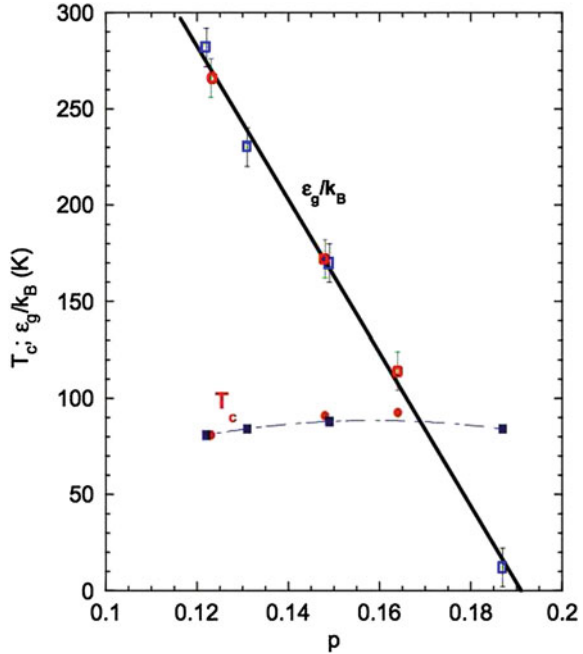


Fig. 2.9 Doping dependent out-of-plane resistivity curves for YBa₂Cu₃O_y. Adapted from Ref. [17], copyright (2011), with permission from Elsevier. *Black* fittings are obtained by theory that presented with the equation given on the graph. *Thin solid line* on $p = 0.123$ and the *arrow* with T^* is plotted additionally to demonstrate the earlier interpretation of the pseudogap in the out-of-plane resistivity, although this method is also consistent with the temperature obtained by this theory

Fig. 2.10 Doping dependence of T_c and ε_g/k_B . Adapted from Ref. [17], copyright (2011), with permission from Elsevier



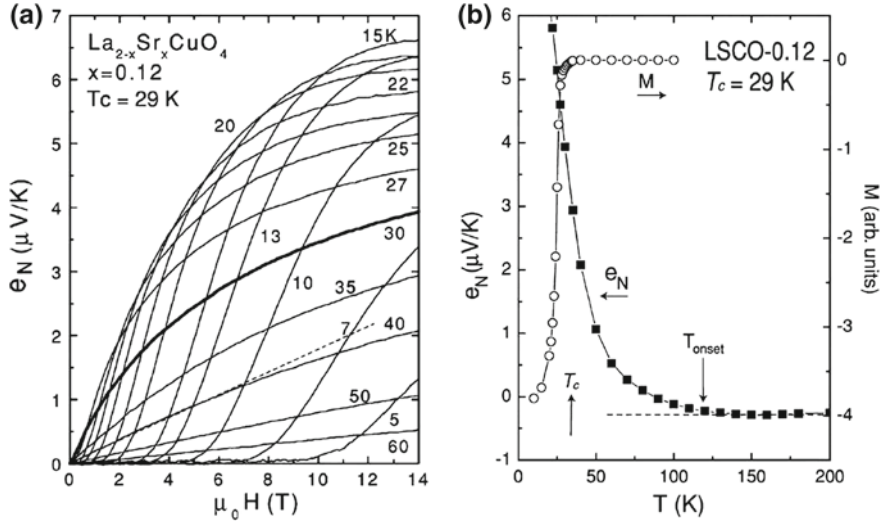


Fig. 2.11 Nernst signal of $\text{La}_{2-x}\text{Sr}_x\text{CuO}_4$ in the underdoped region (a). The Nernst signal also given for this sample. The appearance of the Nernst signal starts well above T_c (b). Reprinted with permission from Ref. [18]. Copyright (2006) by the American Physical Society

superconducting fluctuation regime, yet, there is no consensus about the temperature region and doping dependence of these states.

One of the first experiments that reported the existence of a new temperature region in the phase diagram was Nernst effect measurement [18]. Nernst signal and the temperature dependence are shown in Fig. 2.11. Nernst signal shows a tilted-hill behavior that is generic to the cuprates. In the Nernst experiment, the flow of vortices and antivortices with the applied temperature gradient generates signals with opposite signs. Therefore, the Nernst signal will pick up vorticity. The existence of vortex state can be explained even if the long-range phase coherence disappears with the thermally generated vortices and antivortices. On the other hand, the pair amplitude of the Cooper pairs persists up to very high temperatures. In Fig. 2.12, the region with the enhanced Nernst signal is shown.

Another method that proposed the existence of the precursor superconductivity is the ARPES measurements [19]. Previously, the continuous evolution of the gap feature from superconducting region to the pseudogap had been interpreted as that the pseudogap and superconducting gap have the common origin. On the other hand, the detailed spectral weight analysis of the ARPES signal showed another scale in between T^* and T_c (Fig. 2.13). The doping evolution of this new scale is also straightforward. With decreasing doping level, it has been found that this temperature scale is increasing and clearly shows a different behavior from the pseudogap one. The contributions of the pairing state (T_{pair}) and the pseudogap on to the spectral

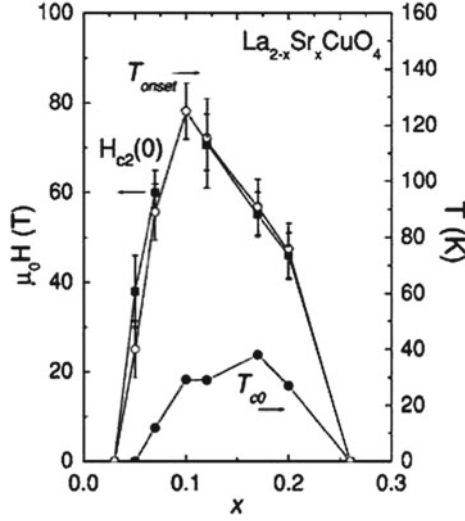


Fig. 2.12 The doping dependence of the Nernst signal for $\text{La}_{2-x}\text{Sr}_x\text{CuO}_4$. Similar behavior also observed for other cuprates. Reprinted with permission from Ref. [18]. Copyright (2006) by the American Physical Society

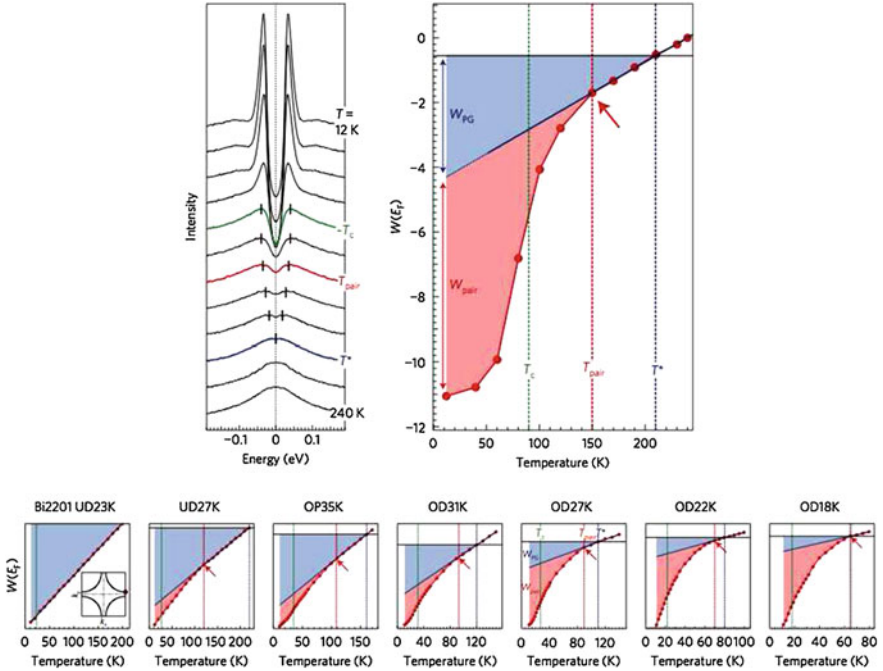


Fig. 2.13 Weighted contributions of the pseudogap and the precursor superconducting state to the ARPES spectral weight. Doping dependence of this state has been given in the *bottom panels*. Reprinted by permission from Macmillan Publishers Ltd: Nature Physics Ref. [19], copyright (2010)

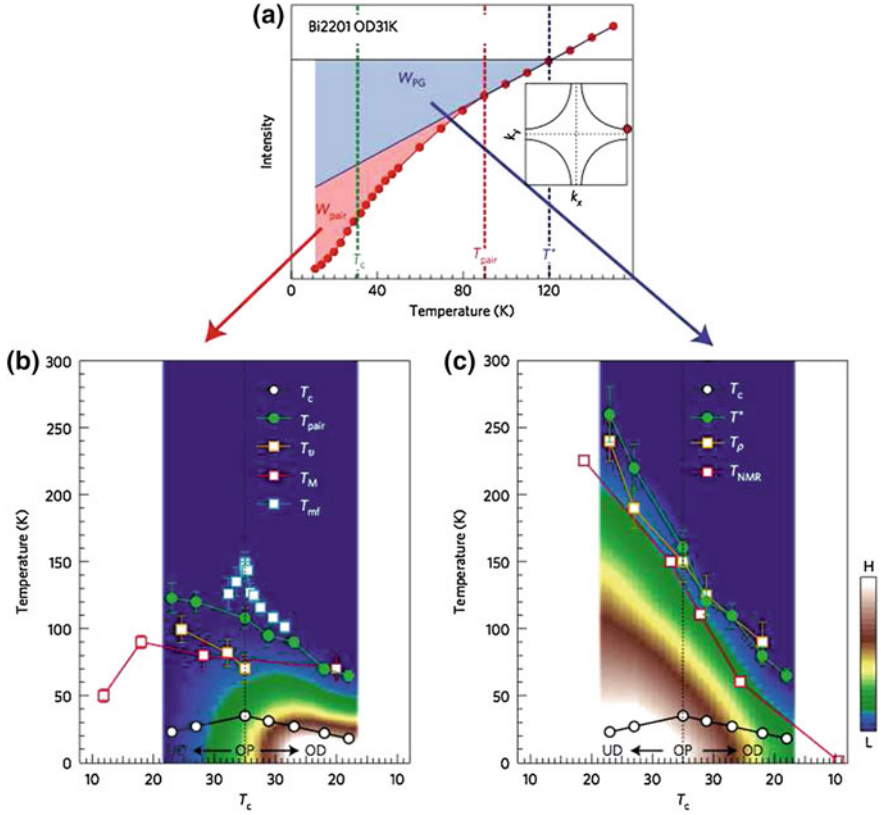


Fig. 2.14 The doping dependence of the precursor state and the pseudogap state. Reprinted by permission from Macmillan Publishers Ltd: Nature Physics Ref. [19], copyright (2010)

weight is shown on the phase diagram in Fig. 2.14. It has been mentioned in this study that the pairing-amplitude and the phase fluctuations are equally important below T_{pair} . Therefore, we cannot interpret this scale as the classically explained superconducting fluctuation regime.

Both ARPES and the Nernst effect measurements show fairly good consistency among them. They both give a precursor state that decreases with increasing doping and extends up to 3–4 T_c as a temperature scale. They are also consistent with other probes such as diamagnetism measurements. If this contribution indeed originates from superconductivity, then it might be explained with a phase separated state [20] or unusually fast vortices [21, 22]. The later one was theoretically proposed, however, such kind of experimental observation has not been reported. Other experiment groups, such as microwave and terahertz, on the other hand, reported a temperature scale that follows the doping dependence of the T_c dome and only extends up to close vicinity of T_c .

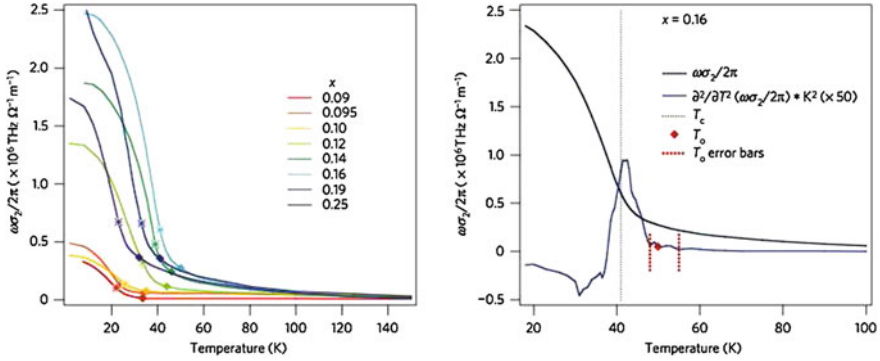


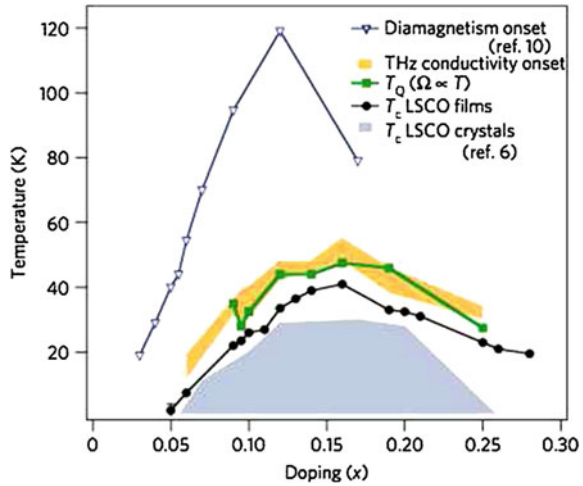
Fig. 2.15 Doping dependent superfluid density curves of $\text{La}_{2-x}\text{Sr}_x\text{CuO}_4$. Asterisks are T_c values, while circles define the precursor state. Right panel shows the obtaining method of the precursor state. Reprinted by permission from Macmillan Publishers Ltd: Nature Physics Ref. [23], copyright (2011)

Terahertz in-plane transmittance measurement was performed on $\text{La}_{2-x}\text{Sr}_x\text{CuO}_4$ cuprate thin films over the entire phase diagram. The superfluid density was calculated by using the imaginary optical conductivity. In Fig. 2.15, the doping dependent variable (related to the superfluid density) as a function of temperature is plotted. As it will be explained later in this thesis, in the result and discussion part, this data also include a normal carrier component. Since the samples are metallic, a Drude component of the normal carriers should be considered in this variable. On the other hand, THz-time domain measurements can only be performed in a low energy (limited) region. Therefore, to determine the normal carrier component is not an easy job and was not done here. Hence, the rapid changes of this variable were taken into account as the indication of the appearance of the superfluid density. The rapid changes were traced with the second derivative of this variable with respect to the temperature.

Analysis in this study showed that the observed region can be explained with usual Ginzburg-Landau formalism [24]. On the other hand, it is significantly different from what was observed in diamagnetism [25] or Nernst effect [18] measurements. A general view has been plotted in Fig. 2.16. One possibility to this discrepancy is that the probes like diamagnetism, etc. might be sensitive to something other than superconductivity. Furthermore, there might be two different kinds of fluctuations, while one of them greatly contribute to the magnetism, the other one may contribute to the conductivity. A convincing explanation has yet to be found.

Microwave measurements also reported similar results to that of THz measurements. In principle, these two methods are similar, where the microwave measurement is more confined to the low energy. However, to obtain the superfluid density (imaginary optical conductivity), we have to assume some theoretical work and analysis. These make the situation more complicated [26].

Fig. 2.16 Phase diagram of $\text{La}_{2-x}\text{Sr}_x\text{CuO}_4$. Comparison with other probes also given. Precursor state does not extend up to very high temperatures and follow T_c dome. Reprinted by permission from Macmillan Publishers Ltd: Nature Physics Ref. [23], copyright (2011)



2.3 General Optical Properties of Cuprates

2.3.1 In-Plane and *c*-Axis Optical Properties

In the last three decades many cuprate families have been discovered. Even though the chemical composition and structure of these families greatly differ from each other, they all have common copper oxide planes, where the superconducting current flows, and a metallic response can be observed within those planes. Transport along the *c*-axis, on the other hand, is significantly different from the in-plane one. It is incoherent in the normal state and originates from the hopping between the copper oxide planes, which gives rise to a semiconducting behavior along the *c*-axis. Below the critical temperature, system becomes superconducting along the *c*-axis due to the Josephson coupling of the conducting planes. Therefore, the conductivity along *c*-axis is orders of magnitude smaller than the conductivity in planes. In Fig. 2.17 the difference between *c*-axis and in-plane transport can be seen clearly. These results belong to one of the prototypical cuprate superconductor $\text{YBa}_2\text{Cu}_3\text{O}_y$ for several oxygen concentrations (*y*).

The optical properties of cuprates also greatly differ in between in-plane and out-of-plane directions. At high energies both spectra reflect the intraband transitions. At low energies, we can observe Drude like behavior along the in-plane of cuprates that reflects the metallic behavior. The electronic component along the in-plane conductivity is very strong, and therefore, the contributions of the phonon effects are difficult to be observed (many cases they are wiped out in the electronic component) and very weak. In contrast, the *c*-axis conductivity is dominated by phonon modes with a weak electronic component. In Fig. 2.18, the generic behaviors of optical conductivity for the in-plane and out-of plane polarization are

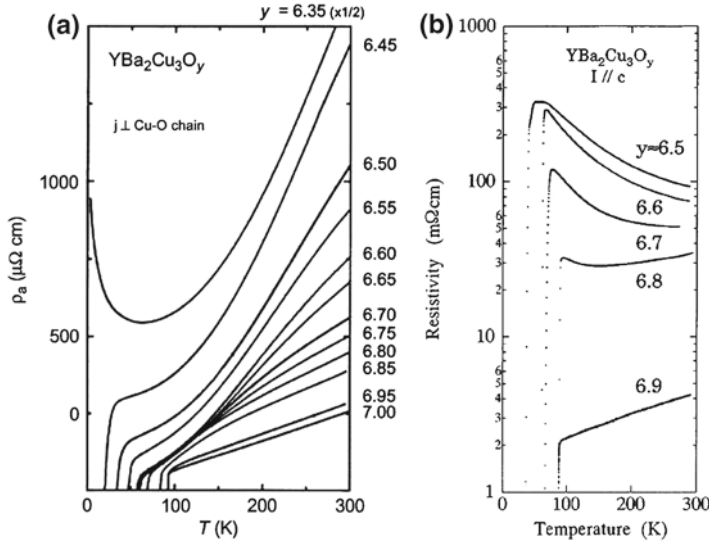


Fig. 2.17 Doping dependent resistivity of $\text{YBa}_2\text{Cu}_3\text{O}_y$ for **a** in-plane and **b** c -axis directions. **a** reprinted from Ref. [27] with kind permission from Springer Science and Business Media and **b** reprinted with permission from Ref. [28]. Copyright (1997) by the American Physical Society

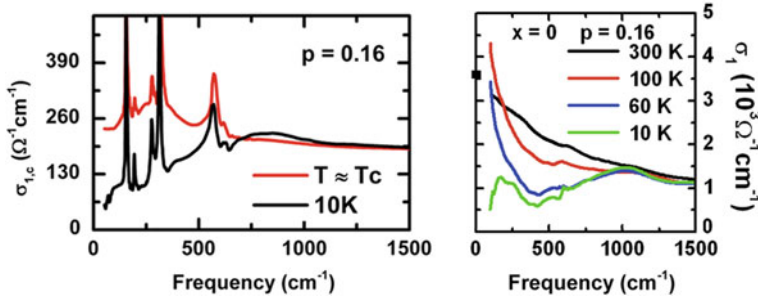
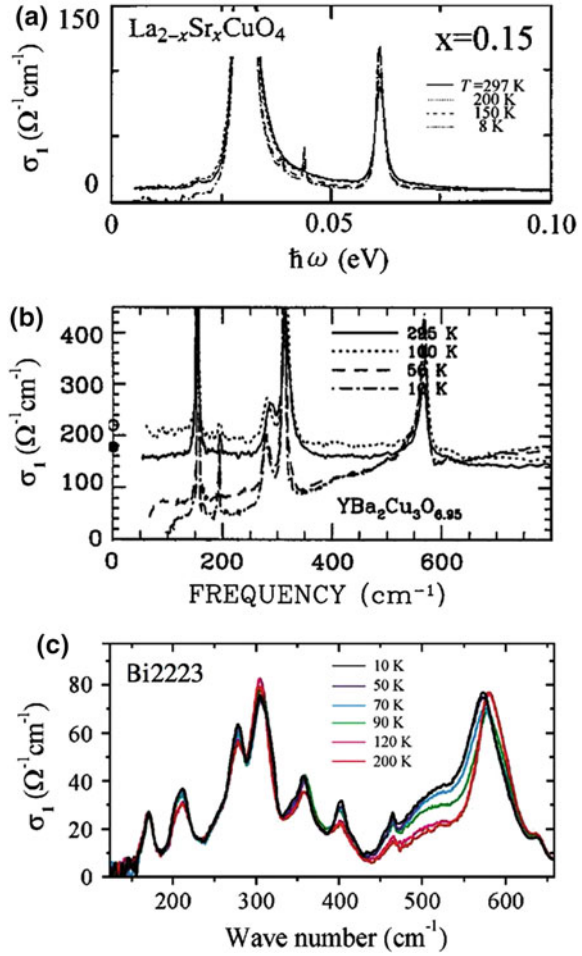


Fig. 2.18 Doping dependent optical conductivity of $\text{YBa}_2\text{Cu}_3\text{O}_y$ for c -axis (*left panel*) and inplane (*right panel*) direction

given. There are many interesting properties of the in-plane response of the cuprate superconductors. But the main topic of this thesis is related with the c -axis properties. Therefore, from now on the general behavior in this polarization will be discussed in more detail.

In-plane conductivity shows metallic behavior over the wide doping region and for all the superconducting samples, c -axis on the other hand, semiconducting for the samples with lower doping. It becomes metallic for the optimally doped and overdoped samples. For $\text{YBa}_2\text{Cu}_3\text{O}_y$ (this sample is special) the c -axis conductivity is higher compared to the other cuprates due to the crystal structure of the $\text{YBa}_2\text{Cu}_3\text{O}_y$, where we know the existence of the CuO chain structure in addition to the CuO_2

Fig. 2.19 Optical conductivity of single layer **a** $\text{La}_{2-x}\text{Sr}_x\text{CuO}_4$, **b** double layer $\text{YBa}_2\text{Cu}_3\text{O}_y$, and **c** trilayer $\text{Bi}_2\text{Sr}_2\text{Ca}_2\text{Cu}_3\text{O}_{10}$. **a** and **c** reprinted with permission from Ref. [29] and [30], respectively. Copyright (1996, 2002) by the American Physical Society. **b** reprinted from Ref. [31], copyright (1995), with permission from Elsevier



planes. Therefore, the hopping between the planes becomes easier due to the chain structures. In $\text{YBa}_2\text{Cu}_3\text{O}_y$ and another class of cuprate $\text{YBa}_2\text{Cu}_4\text{O}_8$ that has a double chain structure, c -axis conductivity is relatively higher than in the other cuprates. In Fig. 2.19, optical conductivity at the optimally doped region is given for a single-, double-, and trilayer cuprate family. As can be seen from this figure, $\text{YBa}_2\text{Cu}_3\text{O}_y$ has the highest conductivity among the cuprates at the same doping level. For instance, the c -axis conductivity at the optimally doped region for $\text{YBa}_2\text{Cu}_3\text{O}_y$ is one order of magnitude higher than the $\text{La}_{2-x}\text{Sr}_x\text{CuO}_4$ at the same doping level. This is one of the reasons why we chose $\text{YBa}_2\text{Cu}_3\text{O}_y$ system to work with in this study, where the details will be explained further in later chapters.

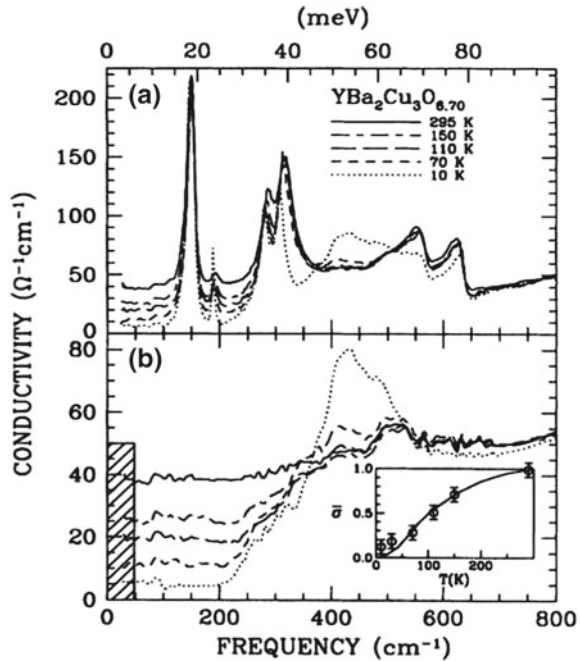
2.3.2 Pseudogap and Superconducting Gap Behavior in *c*-Axis Optical Spectrum

The pseudogap state has been observed by many spectroscopic probes as discussed in Ref. [32]. Optical spectroscopy is an especially powerful probe because it can clearly distinguish a superconducting gap from the insulating gaps. In particular, the *c*-axis polarized optical spectrum is very sensitive to the electronic density of states in the antinodal region [33, 34] of the Fermi surface near $(0, \pi)$ and $(\pi, 0)$, where the pseudogap has a strong effect, while a major pseudogap effect on the in-plane spectra is the reduction of the carrier scattering rate [35]. Therefore, it is possible to observe the pseudogap state more easily in the *c*-axis conductivity ($\sigma_{1,c}(\omega)$) than in the *a*-axis one ($\sigma_{1,a}(\omega)$).

In Fig. 2.20 the optical conductivity spectrum for an underdoped $\text{YBa}_2\text{Cu}_3\text{O}_y$ is shown. T_c of this sample is approximately 70 K. This graph clearly demonstrates the suppression of the low energy optical conductivity that starts much above the superconducting transition. In Fig. 2.20b, the phonon modes are subtracted; therefore, it is easier to see this suppression. Moreover, in the inset of the graph, the conductivity at 50 cm^{-1} normalized with respect to the room temperature conductivity (open circles) is given.

The suppressed spectral weight in the low energy region will be transferred to the high energy region in the pseudogap state. In Fig. 2.21a, the transfer to the high energy

Fig. 2.20 Optical conductivity of underdoped $\text{YBa}_2\text{Cu}_3\text{O}_y$ ($T_c = 70\text{ K}$). **b** shows the same plot after subtracting the phonon modes. *Inset* the conductivity at 50 cm^{-1} normalized with respect to the room temperature conductivity (open circles) together with Knight shift (solid line). Reprinted with permission from Ref. [36]. Copyright (1993) by the American Physical Society



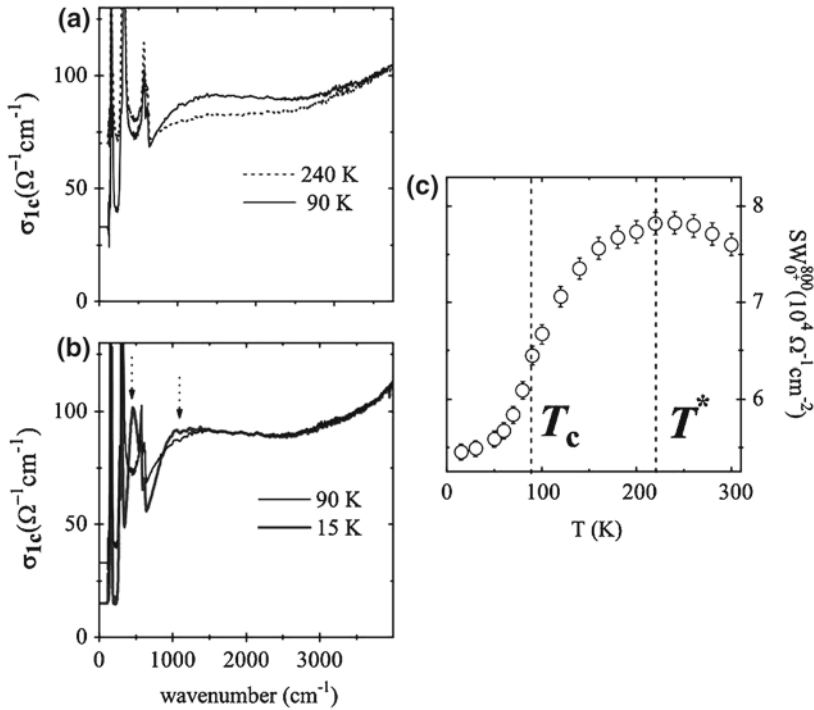


Fig. 2.21 Optical conductivity of underdoped $\text{NdBa}_2\text{Cu}_3\text{O}_y$ ($T_c = 85$ K). **a** High energy transfer with pseudogap opening. **b** Behavior of the superconducting state (Low energy suppression without high energy transfer). **c** shows the spectral weights of specific energy region, $0\text{--}800\text{ cm}^{-1}$. Adapted from Ref. [37] with kind permission from Springer Science and Business Media

region can be seen. In the superconducting state, on the other hand, the low energy optical conductivity is suppressed and it is transferred to the $\delta(0)$. Figure 2.21b shows the superconducting gap behavior. As can be seen from the figure, the low energy conductivity decreases and is lost from the spectrum. The absorption like structures pointed by the arrows in the graph are the structures ascribed to the transverse Josephson plasma (TJP) mode that will be explained in the next section. In Fig. 2.21c, the low energy spectral weight has been calculated which shows the continuous suppression of the low energy conductivity starting from the pseudogap temperature, T^* and continues below T_c .

2.3.3 Superfluid Density in *c*-Axis Optical Spectra

The most significant behavior of the superfluid density in the *c*-axis optical spectrum is the formation of the Josephson plasma edge in the reflectivity spectrum. In Fig. 2.22

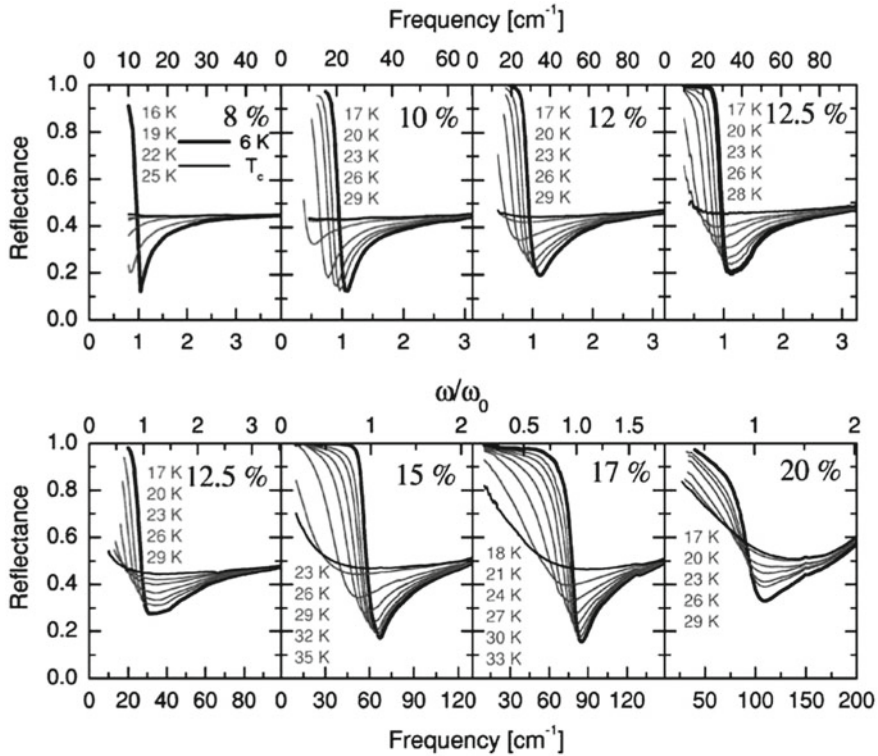


Fig. 2.22 Doping dependent Josephson plasma edge of $\text{La}_{2-x}\text{Sr}_x\text{CuO}_4$. With increasing doping level, the edge position shifts to the higher energies. Reprinted with permission from Ref. [38]. Copyright (2005) by the American Physical Society

the behavior of the Josephson plasma resonance is given for $\text{La}_{2-x}\text{Sr}_x\text{CuO}_4$ for several doping levels. With superconducting transition, the reflectivity at high frequencies starts to drop, which forms a dip and then at lower frequencies it reaches to unity. With decreasing temperature and with increasing doping level, this dip position shifts to the higher energy region. For $\text{La}_{2-x}\text{Sr}_x\text{CuO}_4$ sample this edge position is confined below 100 cm^{-1} , on the other hand for $\text{YBa}_2\text{Cu}_3\text{O}_y$ it might be as high as 300 cm^{-1} . This edge is called Josephson plasma edge, because the study of the doping evolution, etc. led to the conclusion that this feature originates from the Josephson coupling between the CuO_2 planes.

As mentioned previously, the superconducting carriers are condensed to the δ -function at zero frequency, and therefore, the spectral weight that is associated with this δ -peak defines the superfluid density. The density of the condensed electrons can be defined with the penetration depth. A detailed characterization regarding the electrodynamics of the superconducting state will be explained in Chap. 3,

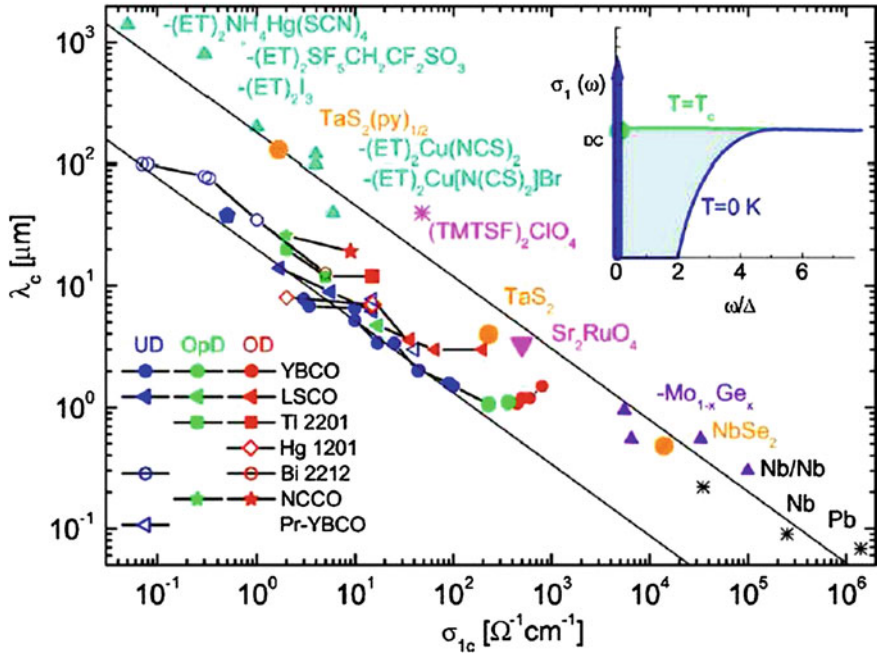


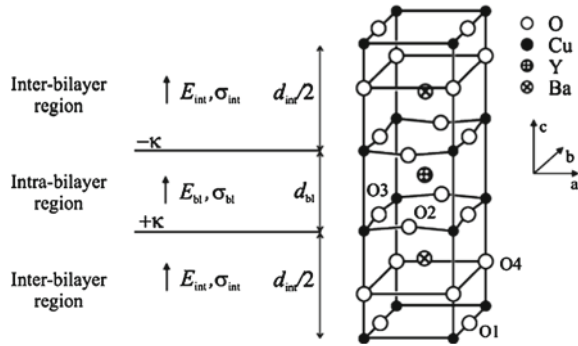
Fig. 2.23 Doping dependence of the penetration depth with respect to dc conductivity. Reprinted with permission from Ref. [45]. Copyright (2005) by the American Physical Society

optical constants section. However, it has been shown that in the case of a Josephson array like c -axis dynamics, the penetration depth can be explained with the relation: $\lambda_c^{-2} \propto \sigma_c$ [39, 40], where indeed this relation had been observed for the c -axis case of the cuprates for a wide doping range. In Fig. 2.23 the general behavior of the penetration depth is shown for several cuprate families. Please note that the penetration depth is calculated from the missing area of the real part of the optical conductivity in this case. Some other theoretical explanations are also proposed [41–44].

2.3.4 Transverse Josephson Plasma (TJP) Resonance Mode

As mentioned previously, c -axis optical conductivity is dominated by the phonon modes at low energy region and reported for many cuprate families. As the superconducting response, the low energy optical conductivity is suppressed and the lost spectral weight is transferred to the δ -function at zero frequency. However, for some of the cuprates, a broad absorption peak was observed around $\sim 400\text{--}500\text{ cm}^{-1}$. Even though, in early studies it has been thought as a phonon mode, in reality it is too broad to be a phonon mode. Later on van der Marel and coworkers proposed an explanation [46] that takes into account of a geometrically separated consecutive

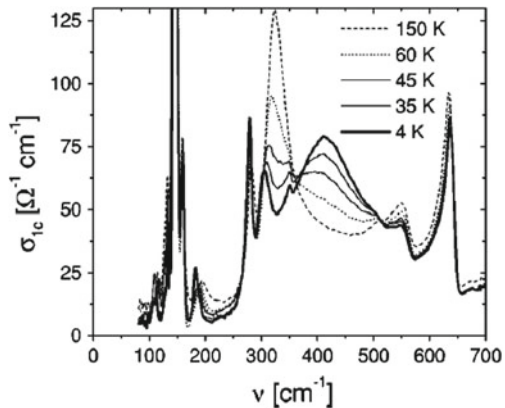
Fig. 2.24 In multilayer compounds the alternating planes causes the TJP mode. Reprinted from Ref. [37] with kind permission from Springer Science and Business Media



metallic layers as shown in Fig. 2.24. There are two different Josephson junctions resonating in the interbilayer and intrabilayer part of the unit cell, which introduces a new transverse mode at finite frequency region in addition to the bulk plasma mode at zero frequency. In this explanation two or more metallic layer compounds are predicted to show an absorption at finite energy region. Indeed, it has been observed for many multilayer cuprate families (two and three layer). Moreover, if the system has alternating different blocking layers, even if the system has only single layer, the TJP resonance mode can be observed (Like in $\text{SmLa}_{1-x}\text{Sr}_x\text{CuO}_{4-d}$ [47]).

This model is very successful to explain the growth of a broad peak in the c -axis spectra, and it can explain the observed phonon anomalies. Especially, the phonon mode resulting from the in-plane oxygen and Cu bending mode is highly affected by the TJP resonance. Originally, this mode was assigned to Josephson currents, and it was thought to appear at T_c , like the Josephson plasma edge. However, later on a careful examination of this mode and the phonon anomalies showed that, in reality it starts to appear at temperatures much higher than the T_c [48], and it has been attributed to the preformed Cooper pairs as a precursor of superconductivity [37, 49]. In Fig. 2.25 the evolution of the absorption peak related to the TJP mode (around 450 cm^{-1}) is shown.

Fig. 2.25 Evolution of the TJP mode in the c -axis optical spectrum. Reprinted with permission from Ref. [48]. Copyright (2000) by the American Physical Society



Beside the observed anomalies on the phonon modes, TJP mode has a complicated behavior. For instance, it has been found that the TJP mode can split in the existence of the phonon modes [50]; some impurity doping such as Zn to Cu sites in the planes can suppress this mode; and in the existence of a magnetic field TJP mode can be suppressed. Moreover, it has been shown that the observed frequency range of the TJP mode is not always the same energy range, but it changes with changing the doping level [48, 51]. This is in a sense is reasonable, since the Josephson plasma edge also shifts in energy region with doping. This is the indication of the change of the superfluid density, just like the Josephson plasma edge. Nonetheless, during the data analysis, it is necessary to be careful.

2.3.5 Impurity Effect on *c*-Axis Optical Properties

It might be preferred to study impurity free systems, when we try to understand the fundamentals of a phenomenon, since introducing impurities may have complicated effects on the observed properties. However, controlled impurities will allow us to obtain some desired properties that may help us to understand the phenomena more easily. Some effects of impurities on cuprate superconductors were studied, and in this section these studies done on *c*-axis optical properties will be summarized.

Impurity effects can be classified into two groups: effects on normal state properties and effects on superconducting state properties. The most common, impurity effect on high temperature cuprate superconductors is the gradual suppression of T_c . Significant effects are observed also in the *c*-axis optical properties.

The first change in the spectrum is the shift of the Josephson plasma edge to the lower energy region with increasing impurities. In Fig. 2.26 this effect is shown for the two cuprate families. This is an expected behavior, since Josephson plasma is the signature of the collective motion of the superconducting carriers in the reflectivity spectra; hence the edge position is related with the superfluid density. Impurities act as pair breakers and decrease the superconducting carrier density, causing a shift of the Josephson plasma edge [52].

Secondly, a change in the TJP resonance mode was observed for the Zn-substituted systems. The softening of the phonon modes related with the TJP resonance mode was also recovered for the Zn-substituted samples. Even though some phonon modes become slightly asymmetric, this difference is negligibly small. This is also surprising especially because the splitting of the phonon band with disorder is expected. In Fig. 2.27, the effect of impurity doping on to TJP mode has been shown.

Another impurity effect on the spectrum can be observed in the overdoped region of the phase diagram. A low energy absorption, so-called residual conductivity at lower energies than the superconducting condensation energy, is observed for many cuprate families [56, 57] (Fig. 2.28). The residual conductivity was observed for both

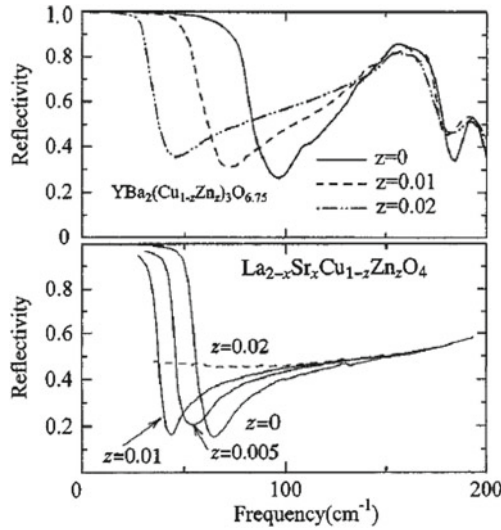


Fig. 2.26 Behavior of the Josephson plasma edge with Zn-substitution for $\text{YBa}_2(\text{Cu}_{1-x}\text{Zn}_x)_3\text{O}_y$ and $\text{La}_{2-x}\text{Sr}_x\text{Cu}_{1-z}\text{Zn}_z\text{O}_4$. Reprinted with permission from Ref. [52]. Copyright (2000) by the American Physical Society

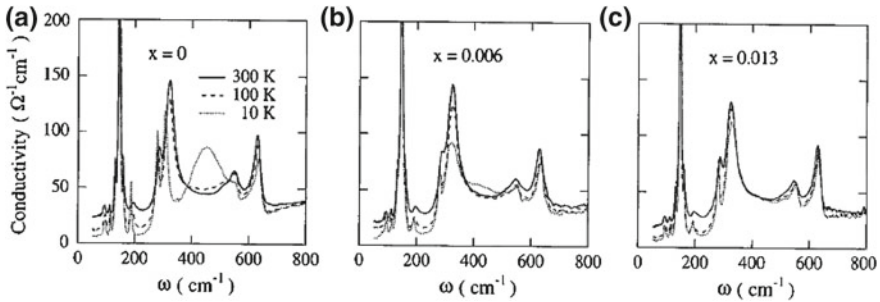


Fig. 2.27 Behavior of the transverse Josephson plasma resonance with Zn-substitution for $\text{YBa}_2(\text{Cu}_{1-x}\text{Zn}_x)_3\text{O}_y$. TJP mode (the absorption band seen at 10 K at around 450cm^{-1}) is suppressed gradually with increasing Zn-content. Reprinted with permission from Ref. [53]. Copyright (1996) by the American Physical Society

in plane and c -axis polarization. It seems that this behavior is intrinsic to the cuprates in the overdoped region. This can be related to the electronic inhomogeneities due to phase separation or pair-breaking occur with the carrier-overdoping. In addition to the intrinsically observed overdoping effect, it is also pointed out that the residual conductivity is increasing with impurity substitution [58], which can be discussed in terms of disorder-induced pair breaking effects.

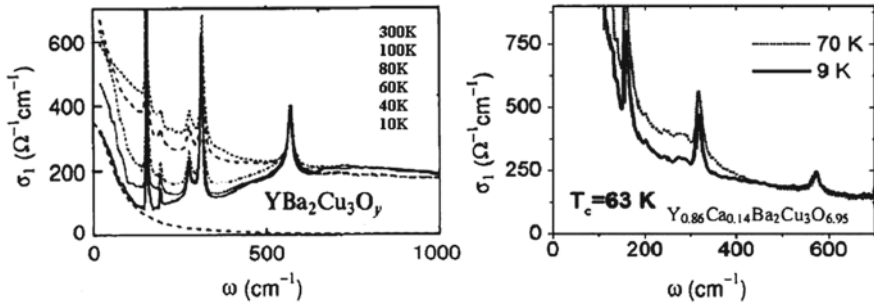


Fig. 2.28 Increase of the residual conductivity with impurity doping (*Left panel*) reprinted from Ref. [54], copyright (1995), with permission from Elsevier. (*right panel*) reprinted with permission from Ref. [55]. Copyright (1998) by the American Physical Society

2.4 Aim of This Study

Despite the variety of the experimental probes and the work done on the pseudogap, there are many questions remained about the content of the pseudogap. The relation of pseudogap with superconductivity; the behavior of the pseudogap in the superconducting region, and the overdoped regime of the phase diagram, still needs to be investigated. In this thesis, the controlled impurities were used to obtain some answers in addition to a systematic doping dependent study. The pseudogap region has been investigated over a wide doping range, in a wide energy region (essential for detailed analysis), and with smaller temperature intervals. So far there has been no systematic study for Zn- and carrier-doping dependence of the c -axis optical spectra, which satisfies all the conditions above.

Moreover, the precursor superconductivity idea should be revisited with more accurate analysis of the data. This motivated us to measure the high and low energy optical spectra for a series of crystals that is thick along c -axis enough for accurate analysis. In many cases, it was difficult to obtain such big crystals; hence measurements were difficult.

Finally, although there are some reports about the kinetic energy driven superconductivity in cuprates for which some pieces of evidence were given by the results of the c -axis infrared spectroscopy, there is no report on this issue for the impurity introduced samples. This systematic study will provide some insight to this topic, as well.

References

1. Dai, P., Chakoumakos, B.C., Sun, G.F., Wong, K.W., Xin, Y., Lu, D.F.: Synthesis and neutron powder diffraction study of the superconductor HgBa₂Ca₂Cu₃O_{8+δ} by Tl substitution. *Physica C* **243**, 201 (1995)
2. Kajitani, T., Hiraga, K., Sakurai, T., Hirabayashi, M., Hosoya, S., Fukuda, T., Oh-Ishi, K.: X-ray and neutron single-crystal diffraction study on La_{1.92}Sr_{0.08}CuO_{4-y}. *Physica C* **171**, 491 (1990)

3. Jorgensen, J.D., Veal, B.W., Paulikas, A.P., Nowicki, L.J., Crabtree, G.B., Claus, H., Kwok, W.K.: Structural properties of oxygen-deficient $\text{YBa}_2\text{Cu}_3\text{O}_{7-\delta}$. *Phys. Rev. B* **41**, 1863 (1990)
4. Emery, V.J.: Theory of high- T_c superconductivity in oxides. *Phys. Rev. Lett.* **58**, 2794 (1988)
5. Varma, C.M., Schmitt-Rink, S., Abraham, E.: Charge transfer excitations and superconductivity in “ionic” metals. *Solid State Commun.* **62**, 681 (1987)
6. Zhang, F.C., Rice, T.M.: Effective hamiltonian for the superconducting Cu oxides. *Phys. Rev. B* **37**, 3759 (1988)
7. Lee, P.A., Nagaosa, N., Wen, X.G.: Doping a mott insulator: physics of high-temperature superconductivity. *Rev. Mod. Phys.* **78**, 17 (2006)
8. Anderson, P.W., Lee, P.A., Randeria, M., Rice, T.M., Trivedi, N., Zhang, F.C.: The physics behind high-temperature superconducting cuprates: the ‘plain vanilla’ version of RVB. *J. Phys.: Condens. Matter* **16**, R755 (2004)
9. Abanov, A., Chubukov, A.V., Schmalian, J.: Quantum-critical theory of the spin-fermion model and its application to cuprates: normal state analysis. *Adv. Phys.* **52**, 119 (2003)
10. Chubukov, A.V., Morr, D.K.: Electronic structure of underdoped cuprates. *Phys. Rep.* **288**, 355 (1997)
11. Kivelson, S.A., Bindloss, I.P., Fradkin, E., Tranquada, J.M., Kapitulnik, A., Howald, C.: How to detect fluctuating stripes in the high-temperature superconductors. *Rev. Mod. Phys.* **75**, 1201 (2003)
12. Takigawa, M., Reyes, A.P., Hammel, P.C., Thompson, J.D., Heffner, R.H., Fisk, Z., Ott, K.C.: Cu and O NMR studies of the magnetic properties of $\text{YBa}_2\text{Cu}_3\text{O}_{6.63}$ ($T_c = 62$ K). *Phys. Rev. B* **43**, 247 (1991)
13. Alloul, H., Ohno, T., Mendels, P.: ^{89}Y NMR evidence for a fermi liquid behavior in $\text{YBa}_2\text{Cu}_3\text{O}_{6+x}$. *Phys. Rev. Lett.* **63**, 1700 (1989)
14. Sato, T., Matsui, H., Nishina, S., Takahashi, T., Fujii, T., Watanabe, T., Matsuda, A.: Low energy excitation and scaling in $\text{Bi}_2\text{Sr}_2\text{Ca}_{n-1}\text{Cu}_n\text{O}_{2n+4}$ ($n = 1-3$): angle-resolved photoemission spectroscopy. *Phys. Rev. Lett.* **89**, 067005 (2002)
15. Vishik, I.M., Lee, W.S., He, R.H., Hashimoto, M., Hussain, Z., Devereaux, T.P., Shen, Z.X.: Arpes studies of cuprate fermiology: superconductivity, pseudogap and quasiparticle dynamics. *New J. Phys.* **12**, 105008 (2010)
16. Ando, Y., Komiya, S., Segawa, K., Ono, S., Kurita, Y.: Electronic phase diagram of high- T_c cuprate superconductors from a mapping of the in-plane resistivity curvature. *Phys. Rev. Lett.* **93**, 267001 (2004)
17. Naqib, S., Uddin, M.B., Cole, J.: Modeling of the out-of-plane resistivity of cuprate superconductors. *Physica C* **471**, 1598 (2011)
18. Wang, Y., Li, L., Ong, N.P.: Nernst effect in high- T_c superconductors. *Phys. Rev. B* **73**, 024510 (2006)
19. Kondo, T., Hamaya, Y., Palczewski, A.D., Takeuchi, T., Wen, J.S., Xu, Z.J., Gu, G., Schmalian, J., Kaminski, A.: Disentangling cooper-pair formation above the transition temperature from the pseudogap state in the cuprates. *Nat. Phys.* **7**, 21 (2010)
20. Martin, I., Panagopoulos, C.: Nernst effect and diamagnetic response in a stripe model of superconducting cuprates. *Europhys. Lett.* **91**, 67001 (2010)
21. Ioffe, L.B., Millis, A.J.: Big fast vortices in the d-wave resonating valence bond theory of high-temperature superconductivity. *Phys. Rev. B* **66**, 094513 (2002)
22. Lee, P.A.: Orbital currents and cheap vortices in underdoped cuprates. *Physica C* **388**, 7 (2003)
23. Bilbro, L.S., Aguilar, R.V., Logvenov, G., Pelleg, O., Božović, I., Armitage, N.P.: Temporal correlations of superconductivity above the transition temperature in $\text{La}_{2-x}\text{Sr}_x\text{CuO}_4$ probed by terahertz spectroscopy. *Nat. Phys.* **7**, 298 (2011)
24. Larkin, A., Varlamov, A.: *Theory of Fluctuations in Superconductors*. Oxford Science Publications, Oxford (2005)
25. Li, L., Wang, Y., Komiya, S., Ono, S., Ando, Y., Gu, G.D., Ong, N.P.: Diamagnetism and cooper pairing above T_c in cuprates. *Phys. Rev. B* **81**, 054510 (2010)
26. Grbić, M.S., Požek, M., Paar, D., Hinkov, V., Raichle, M., Haug, D., Keimer, B., Barišić, N., Dulčić, A.: Temperature range of superconducting fluctuations above T_c in $\text{YBa}_2\text{Cu}_3\text{O}_{7-\delta}$ single crystals. *Phys. Rev. B* **83**, 144508 (2011)

27. Segawa, K., Ando, Y.: Transport properties of untwinned $\text{YBa}_2\text{Cu}_3\text{O}_y$ single crystals and the origin of the 60-K plateau. *J. Low Temp. Phys.* **131**, 821 (2003)
28. Tajima, S., Schützmann, J., Miyamoto, S., Terasaki, I., Sato, Y., Hauff, R.: Optical study of c -axis charge dynamics in $\text{YBa}_2\text{Cu}_3\text{O}_y$: carrier self-confinement in the normal and the superconducting states. *Phys. Rev. B* **55**, 6051 (1997)
29. Uchida, S., Tamasaku, K., Tajima, S.: c -axis optical spectra and charge dynamics in $\text{La}_{2-x}\text{Sr}_x\text{CuO}_4$. *Phys. Rev. B* **53**, 14558 (1996)
30. Boris, A., Munzar, D., Kovaleva, N.N., Liang, B., Lin, C.T., Dubroka, A., Pimenov, A., Holden, T., Keimer, B., Mathis, Y.L., Bernhard, C.: Josephson plasma resonance and phonon anomalies in trilayer $\text{Bi}_2\text{Sr}_2\text{Ca}_2\text{Cu}_3\text{O}_{10}$. *Phys. Rev. Lett.* **89**, 277001 (2002)
31. Homes, C.C., Timusk, T., Bonn, D.A., Liang, R., Hardy, W.N.: Optical properties along the c -axis of $\text{YBa}_2\text{Cu}_3\text{O}_{6+x}$, for $x = 0.50$ to 0.95 evolution of the pseudogap. *Physica C* **254**, 265 (1995)
32. Timusk, T., Statt, B.: The pseudogap in high-temperature superconductors: an experimental survey. *Rep. Prog. Phys.* **62**, 61 (1996)
33. Ioffe, L.B., Millis, A.J.: Superconductivity and the c -axis spectral weight of high- T_c superconductors. *Science* **285**, 1241 (1999)
34. Chakravarty, S., Sudbo, A., Anderson, P.W., Strong, S.: Interlayer tunneling and gap anisotropy in high-temperature superconductors. *Science* **261**, 337 (1993)
35. Puchkov, A.V., Basov, D.N., Timusk, T.: The pseudogap state in high- T_c superconductors: an infrared study. *J. Phys.: Condens. Matter* **8**, 10049 (1996)
36. Homes, C.C., Timusk, T., Liang, R., Bonn, D.A., Hardy, W.N.: Optical conductivity of c -axis oriented $\text{YBa}_2\text{Cu}_3\text{O}_{6.70}$: evidence for a pseudogap. *Phys. Rev. Lett.* **71**, 1645 (1993)
37. Dubroka, A., Yu, L., Munzar, D., Kim, K.W., Rössle, M.R., Malik, V.K., Lin, C.T., Keimer, B., Wolf, T., Bernhard, C.: Pseudogap and precursor superconductivity pseudogap and precursor superconductivity in underdoped cuprate high temperature superconductors: A far-infrared ellipsometry study. *Eur. Phys. J. Spec. Top.* **188**, 73 (2010)
38. Dordevic, S.V., Komiya, S., Ando, Y., Wang, Y.J., Basov, D.N.: Josephson vortex state across the phase diagram of $\text{La}_{2-x}\text{Sr}_x\text{CuO}_4$: a magneto-optics study. *Phys. Rev. B* **71**, 054503 (2005)
39. Basov, D.N., Timusk, T., Dabrowski, B., Jorgensen, J.D.: c -axis response of $\text{YBa}_2\text{Cu}_4\text{O}_8$: a pseudogap and possibility of Josephson coupling of CuO_2 planes. *Phys. Rev. B* **50**, 3511 (1994)
40. Shibauchi, T., Kitano, H., Uchinokura, K., Maeda, A., Kimura, T., Kishio, K.: Anisotropic penetration depth in $\text{La}_{2-x}\text{Sr}_x\text{CuO}_4$. *Phys. Rev. Lett.* **72**, 2263 (1994)
41. Hirschfeld, P.J., Quinlan, S.M., Scalapino, D.J.: c -axis infrared conductivity of a $d_{x^2-y^2}$ wave superconductor with impurity and spin-fluctuation scattering. *Phys. Rev. B* **55**, 12742 (1997)
42. Chakravarty, S., Kee, H.Y., Abrahams, E.: Frustrated kinetic energy, the optical sum rule, and the mechanism of superconductivity. *Phys. Rev. Lett.* **82**, 2366 (1999)
43. Kim, W., Carbotte, J.P.: Conductivity sum rule: comparison of coherent and incoherent c -axis coupling. *Phys. Rev. B* **61**, 11886(R) (2000)
44. Ohashi, Y.: Theory of Basov correlation between penetration depth and conductivity along the c -axis in high- T_c cuprate superconductors. *J. Phys. Soc. Jpn.* **69**, 659 (2000)
45. Basov, D.N., Timusk, T.: Electrodynamics of high- T_c superconductors. *Rev. Mod. Phys.* **77**, 721 (2005)
46. van der Marel, D., Tsvetkov, A.A.: Transverse optical plasmons in layered superconductors. *Czech. J. Phys.* **46**, 3165 (1996)
47. Shibata, H., Yamada, T.: Double Josephson plasma resonance in T^* phase $\text{SmLa}_{1-x}\text{Sr}_x\text{CuO}_{4-\delta}$. *Phys. Rev. Lett.* **81**, 3519 (1998)
48. Bernhard, C., Munzar, D., Golnik, A., Lin, C.T., Wittlin, A., Humlíček, J., Cardona, M.: Anomaly of oxygen bond-bending mode at 320 cm^{-1} and additional absorption peak in the c -axis infrared conductivity of underdoped $\text{YBa}_2\text{Cu}_3\text{O}_{7-\delta}$ single crystals revisited with ellipsometric measurements. *Phys. Rev. B* **61**, 618 (2000)
49. Grüninger, M., van der Marel, D., Tsvetkov, A.A., Erb, A.: Observation of out-of-phase bilayer plasmons in $\text{YBa}_2\text{Cu}_3\text{O}_{7-\delta}$. *Phys. Rev. Lett.* **84**, 1575 (2000)

50. Munzar, D., Holden, T., Bernhard, C.: Approximate tight-binding sum rule for the superconductivity-related change of c -axis kinetic energy in multilayer cuprate superconductors. *Phys. Rev. B* **67**, 020501(R) (2003)
51. Dubroka, A., Munzar, D.: Phonon anomalies in trilayer high- T_c cuprate superconductors. *Physica C* **405**, 133 (2004)
52. Fukuzumi, Y., Mizuhashi, K., Uchida, S.: Zn-doping effect on the c -axis charge dynamics of underdoped high- T_c cuprates. *Phys. Rev. B* **61**, 627 (2000)
53. Hauff, R., Tajima, S., Jang, W.J., Rykov, A.I.: Optical study on phonon anomalies and spin gap in $\text{YBa}_2(\text{Cu}_{1-x}\text{Zn}_x)_3\text{O}_{6.6}$. *Phys. Rev. Lett.* **77**, 4620 (1996)
54. Schützmann, J., Tajima, S., Miyamoto, S., Sato, Y., Terasaki, I.: Origin of low-temperature residual absorption in $\text{YBa}_2\text{Cu}_3\text{O}_y$. *Solid State Commun.* **94**, 293 (1995)
55. Bernhard, C., Henn, R., Wittlin, A., Kläser, M., Wolf, T., Müller-Vogt, G., Lin, C.T., Cardona, M.: Electronic c -axis response of $\text{Y}_{1-x}\text{Ca}_x\text{Ba}_2\text{Cu}_3\text{O}_{7-\delta}$ crystals studied by far-infrared ellipsometry. *Phys. Rev. Lett.* **80**, 1762 (1998)
56. Tajima, S., Fudamoto, Y., Kakeshita, T., Gorshunov, B., Zélezny, V., Kojima, K.M., Dressel, M., Uchida, S.: In-plane optical conductivity of $\text{La}_{2-x}\text{Sr}_x\text{CuO}_4$: reduced superconducting condensate and residual Drude-like response. *Phys. Rev. B* **71**, 094508 (2005)
57. Ma, Y.C., Wang, N.L.: Infrared scattering rate of overdoped $\text{Tl}_2\text{Ba}_2\text{CuO}_{6+\delta}$. *Phys. Rev. B* **73**, 144503 (2006)
58. Uykur, E., Tanaka, K., Masui, T., Miyasaka, S., Tajima, S.: In-plane optical spectra of $\text{Y}_{1-x}\text{Ca}_x\text{Ba}_2\text{Cu}_3\text{O}_{7-\delta}$: overdoping and disorder effects on residual conductivity. *Phys. Rev. B* **84**, 184527 (2011)

Pseudogap and Precursor Superconductivity Study of
Zn doped YBCO

Uykur, E.

2015, XIII, 93 p. 79 illus., 54 illus. in color., Hardcover

ISBN: 978-4-431-55509-4